Geophysical Research Letters

RESEARCH LETTER
10.1029/2019GL084041

Segmentation of SED by Boundary Flows Associated With Westward Drifting Partial Ring current

Zihan Wang[1], Shasha Zou[1], Thomas Coppeans[1], Jiaen Ren[1], Aaron Ridley[1], and Tamas Gombosi[1]

[1]Department of Climate and Space Sciences and Engineering, University of Michigan, Ann Arbor, MI, USA

Key Points:
- Boundary flows between Region 1 and Region 2 FACs segment SED plume into patches
- Localized plasma loss is due to enhanced frictional heating within boundary flows
- No external IMF direction change is needed in this segmentation scenario

Supporting Information:
- Supporting Information S1

Correspondence to:
Z. Wang,
wzihan@umich.edu

Citation:
Wang, Z., Zou, S., Coppeans, T., Ren, J., Ridley, A., & Gombosi, T. (2019). Segmentation of SED by boundary flows associated with westward drifting partial ring current. *Geophysical Research Letters*, *46*, 7920–7928. https://doi.org/10.1029/2019GL084041

Received 7 JUN 2019
Accepted 16 JUL 2019
Accepted article online 22 JUL 2019
Published online 26 JUL 2019

Abstract The segmentation mechanism of polar cap patches is agreed to be related to temporal changes of interplanetary magnetic field or transient reconnection. In this letter, using Global Ionosphere Thermosphere Model driven by two-way coupled Block-Adaptive-Tree-Solarwind-Roe-Upwind-Scheme and Rice Convection Model, a new segmentation mechanism is proposed. This mechanism works as follows: A strong boundary flow between the Region 1 and Region 2 field-aligned currents develops, while a shielding process develops in the inner magnetosphere. As the partial ring current drifts westward, the peak of the boundary flow also moves westward. This strong boundary flow raises the ion temperature through enhanced frictional heating, enhances the chemical recombination reaction rate, and reduces the electron density. When this boundary flow crosses the storm-enhanced density (SED) plume, the plume will be segmented into patches. No external interplanetary magnetic field variations or transient reconnections are required in this mechanism.

1. Introduction

Polar cap patches are high *F*-region plasma density structures in the polar cap where the density is much higher than the background level. Both storm-enhanced density (SED) and patches have drawn much attention since their discoveries, because the large density gradient at their edges is favorable for ionospheric irregularities to develop. Thus, they are the major space weather concern in the polar cap that can disrupt navigation and communication signals during times of geomagnetic disturbance.

Various formation mechanisms of patch segmentation have been proposed, and it is still controversial which mechanism is the dominant one. However, it is typically believed that the formation of patch needs a reservoir of high-density plasma and a segmentation mechanism. There are two sources of high-density plasma: The first source is the plasma density increase in the cusp due to soft precipitation in the *F* region (Goodwin et al., 2015; Rodger et al., 1994; Walker et al., 1999). The second source is the dense thermal plasma from the sunlit region (Anderson et al., 1988). SED is a ridge of enhanced electron density in the midlatitude region that forms during storm time (Foster, 1993) and is considered to be an important plasma source for patches. Ren et al. (2018) show that the altitude profiles of patch density and temperature resemble those of SED. That is, the patch density is usually higher than the sector median above 200 km and lower than that below 200 km, and the patch electron temperature is lower than the surrounding region. This is strong evidence that patches originate from SED.

The dense plasma of SED can be transported into the high-latitude region to form SED plume or tongue of ionization (Foster, 1984). To isolate the plume into patches, a segmentation mechanism is needed. It is generally believed that the segmentation is closely related with interplanetary magnetic field (IMF) variations. Patches can be segmented due to the temporal changes in both IMF *Bz* (Anderson et al., 1988) and *By* (Milan et al., 2002; Sojka et al., 1993). Patches can also be generated by flux transfer events near the cusp region (Carlson et al., 2004; Carlson et al., 2006; Lockwood & Carlson, 1992). Flux transfer event can lead to mesoscale (about 100 km) fast flow channels near the cusp (Oksavik et al., 2006; Pinnock et al., 1993) and then bring dense plasma into the polar cap region (Lockwood & Carlson, 1992; Rodger et al., 1994; Zhang et al., 2011). Moen et al. (2006) further show that pulsed return flow due to transient reconnection can chop the plume into patches in the subauroral region. Another possibility is that fast flow jets due to transient reconnection produce high-temperature and low-density plasma through frictional heating and erode the preexisting plume into patches (Ogawa et al., 2001; Valladares et al., 1994; Valladares et al., 1996). Zhang

et al. (2013) further show that the low-density plasma due to precipitation can segment the tongue of ionization into patches during transient reconnection. Zhang et al. (2016) show that Subauroral Polarization Streams can transport low-density plasma from the nightside to cut the SED during a substorm.

In this letter, Global Ionosphere Thermosphere Model (GITM) was used to simulate the geomagnetic storm on 7 September 2017 and study the segmentation of SED plume into a polar cap patch. GITM is driven by high-resolution coupled Block-Adaptive-Tree-Solar Wind-Roe-Upwind-Scheme (BATSRUS) and Rice Convection Model (RCM) within the Space Weather Modeling Framework (SWMF; Tóth et al., 2005, 2012). Our results not only are consistent with observations but also for the first time show that a strong boundary flow can form between the Region 1 and Region 2 field-aligned currents (FACs) during the shielding development and westward drift of partial ring current in the inner magnetosphere, and this flow can reduce the electron density and segment SED plume into a patch.

2. Observations and Modeling

2.1. Model Description

GITM is a three-dimensional spherical grid that models the Earth's global ionosphere and thermosphere system self-consistently (Ridley et al., 2006). In this study, the spatial resolution of GITM is set to 1° in latitude and 2° in longitude with 50 vertical levels (from ~100 to ~700 km). GITM allows different models of high-latitude electric fields, auroral particle precipitation, and solar radiation as inputs. In this study, the Flare Irradiance Spectral Model (FISM; Chamberlin et al., 2007, 2008) is used to provide solar irradiance input for the whole simulation. FISM is an empirical model of the solar irradiance spectrum covering from 0.1 to 190 nm with 1-nm resolution and 1-min temporal resolution. Using the high-resolution FISM model, the solar flare impact on the ionosphere and thermosphere can be captured.

Various models of high-latitude electric fields and auroral particle precipitation can be used in GITM. At first, GITM was run for two quiet days (4–5 September) to achieve steady state. During this stage, the Fuller-Rowell and Evans (1987) empirical model and Weimer (2005) empirical electric field model are used as the precipitation and electric field input, respectively. The Fuller-Rowell and Evans model is driven by hemispheric power, which is found to be linearly related with $AL^{1/2}$ in Østgaard et al. (2002) empirical model. We use the observed AL index from the Kyoto World Data Center to calculate the hemispheric power. The Weimer model is driven by the observed solar wind data from OMNIWeb. Starting from 6 September 00 UT, the high-latitude driver is switched to the electric field and precipitation from the two-way coupled BATSRUS and RCM, as part of the University of Michigan SWMF (De Zeeuw et al., 2004; Tóth et al., 2012). The coupled model is driven by the real solar wind data from OMNIWeb. High-resolution grid (1/8 R_E) in the inner magnetosphere, magnetopause, and current sheet has been implemented to better capture dynamic FACs and precipitation structures.

2.2. Solar Wind and IMF

An intense double-dip geomagnetic storm occurred at 7–8 September 2017 and has received much attention (e.g., Aa et al., 2018; Jin et al., 2018). The SYM-H index reached −142 nT during the first dip and then ~ −100 nT during the second dip. The double-dip storm was driven by multiple interplanetary coronal mass ejections (ICMEs) passing the Earth successively (Shen et al., 2018). From top to bottom, Figures 1a–1f show the IMF *By*, *Bz* in geocentric solar magnetospheric coordinates, solar wind speed, proton number density, dynamic pressure, and the SYM-H index during 7–8 September 2017. The IMF *Bz* turned southward at ~2040 UT on 7 September due to the arrival of the first ICME, leading to the initial decrease of SYM-H. At ~2330 UT, a shock-ICME complex structure arrived with the shock enhanced IMF *Bz* reaching ~ −30 nT. A sudden storm commencement signaled by the sudden SYM-H increase was also initiated by this shock. After that, the SYM-H continued to decrease due to the large southward IMF and reached the first minimum at ~0100 UT. Then the storm began to recover until the arrival of another ICME at ~1105 UT on 8 September, which led to the second main phase. In this study, we focus on the development and structuring of SED during the first main phase. In Figure 1f, the dashed line represents the simulated Dst index. Although there is a ~20-nT negative bias, the temporal variation of the simulated Dst is consistent with the SYM-H index.

2.3. Model Results

The SED formation and patch segmentation processes are shown in Figure 2, and the color-coded vertical dashed lines in Figure 1 indicate the timing of the three snapshots (2100, 2130, and 2300 UT). The first row shows the GPS total electron content (TEC) in geomagnetic coordinates. It is shown that the SED and the

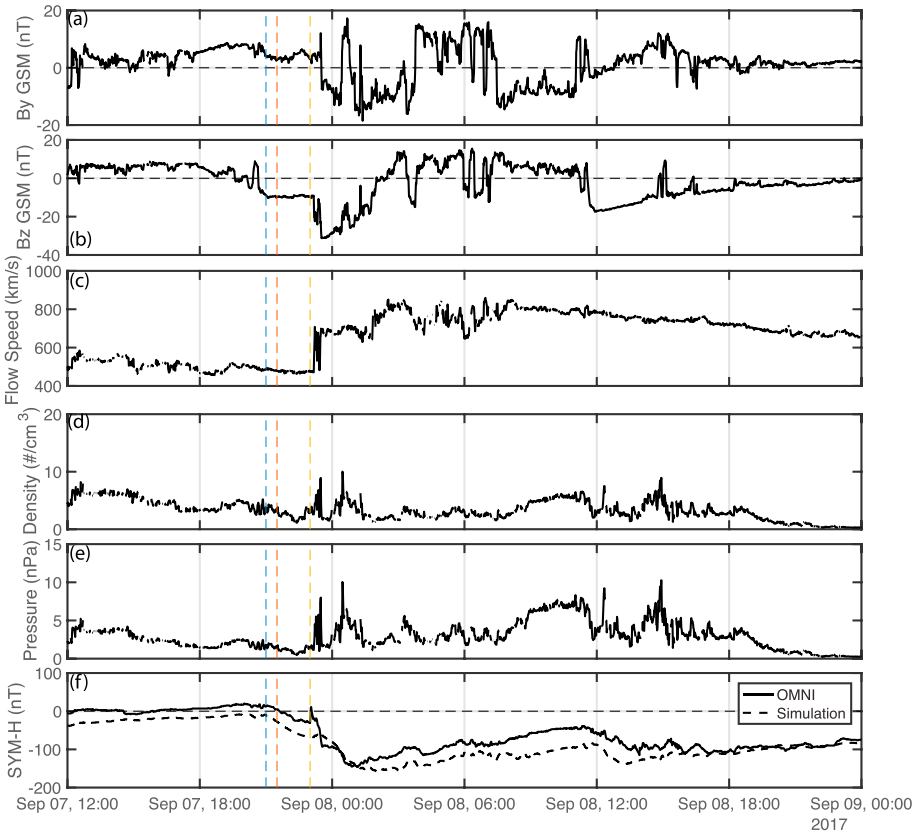

Figure 1. Solar wind data and geomagnetic index from 12 UT 7 September to 0 UT 9 September 2017. (a) IMF By component in the GSM coordinates, (b) IMF *Bz* component in the GSM coordinates, (c) solar wind speed, (d) proton number density, (e) solar wind dynamic pressure, and (f) the SYM-H index (solid line) and simulated Dst index (dashed line). The color-coded vertical dashed lines indicate timing of the three snapshots in Figure 2. GSM = geocentric solar magnetospheric; IMF = interplanetary magnetic field.

plume began to develop after the southward turning of IMF, and the segmentation of the plume occurred at 2300 UT. The bottom three rows in Figure 2 show the dynamical evolution of the ionosphere and inner magnetosphere from SWMF after the first southward turning. The second row shows the GITM electron density at 349.4 km with color contours and electric equipotential line contours every 10^4 V in geomagnetic coordinates centered at the magnetic North Pole. The third row shows the SWMF FACs with color contours and the same electric equipotential contours every 10^4 V in geomagnetic coordinates. The green dashed line represents the open-closed field line boundary (OCB). The bottom row shows the plasma pressure in the *XY* plane at $Z = 0$ in geocentric solar magnetospheric coordinates. Movies of GPS TEC, electron density at 350 km, FACs, and plasma thermal pressure are provided in the supporting information. Based on the comparison between the first and second row in Figure 2, it is shown that the simulation results successfully captured the development of the SED and plume after 2100 UT, and the segmentation of plume at 2300 UT.

As shown in Figure 1, the IMF *Bz* turned southward at 2040 UT on 7 September, reaching −10 nT at 2100 UT, and stayed steadily southward for about 2.5 hr until the shock arrival at 2330 UT. Due to this southward turning, a two-cell convection pattern started to form and the convection electric field penetrated to midlatitudes. The convection also tilted toward the dawnside, which is likely due to the long-lasting positive IMF *By* (Weimer, 2005). In the equatorial plane of the inner magnetosphere, a weak nearly symmetric ring current can be seen at 21 UT. Both the Region 1 and Region 2 FACs existed. However, the Region 2 FACs were weaker than the Region 1 FACs because of weak partial ring current. The penetrated electric field was able to reach the plasma in the sunlit midlatitude region. Both the two-cell convection pattern and OCB expanded to lower latitude. More plasma in the midlatitude followed the convection to higher latitude. Because the magnetic field is not strictly vertical in subauroral and auroral region, the convection flow had an upward component and transported plasma to higher altitude, where the charge exchange and recombination rate

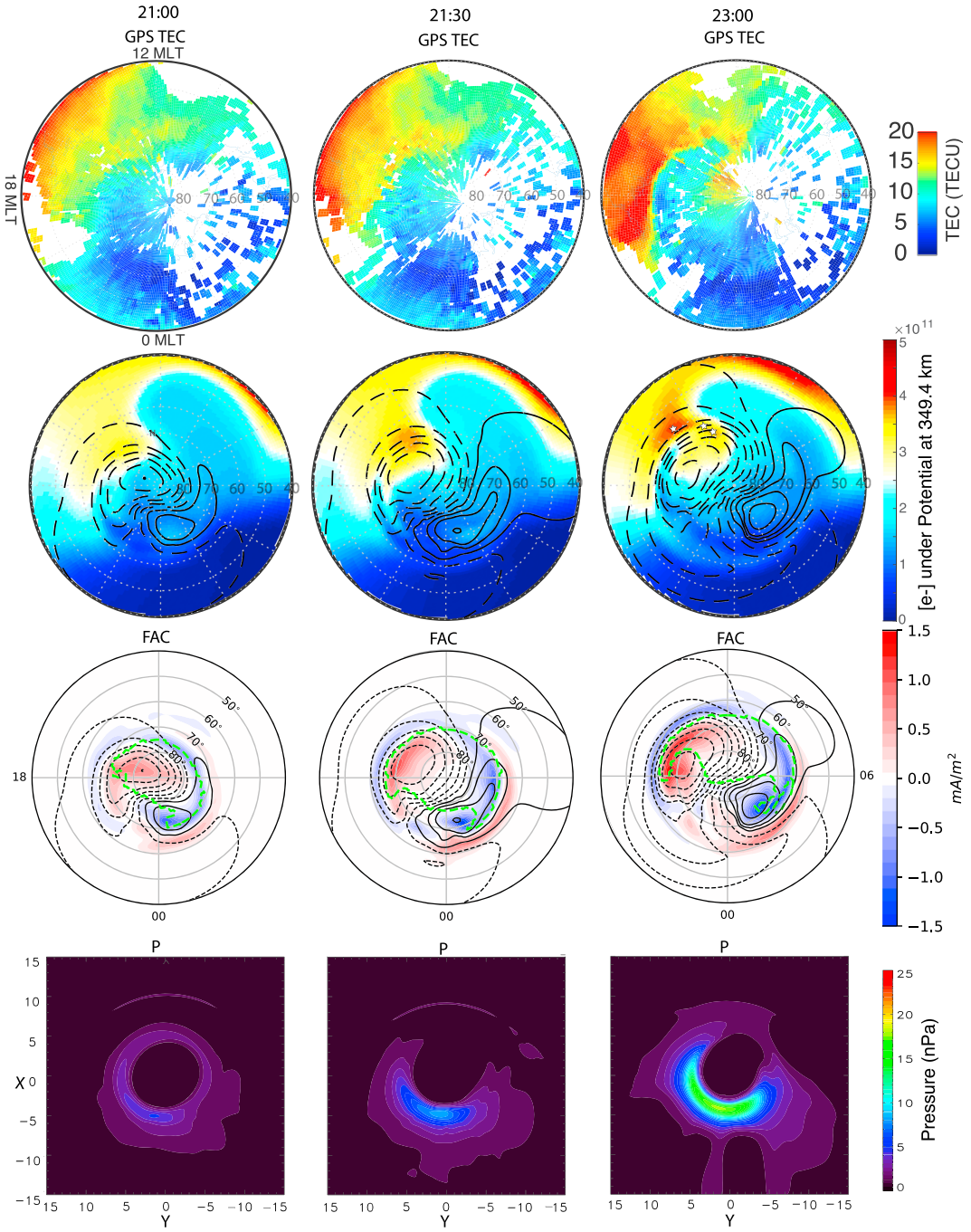

Figure 2. (first row) Polar view of TEC in the geomagnetic coordinates. (second row) Polar view of modeled electron density (color contours) at 349.4 km under electric equipotential (contour lines) in the geomagnetic coordinates. The storm-enhanced density base, boundary flow, and polar cap patch are marked with stars at 23 UT. (third row) Polar view of the modeled FACs (color contours) under electric equipotential (contour lines) in the geomagnetic coordinates. The green dashed line represents the open-closed field line boundary. (fourth row) The modeled plasma thermal pressure in the $z = 0$ plane in the geocentric solar magnetospheric coordinates. FAC = field-aligned current; MLT = magnetic local time; TEC = total electron content.

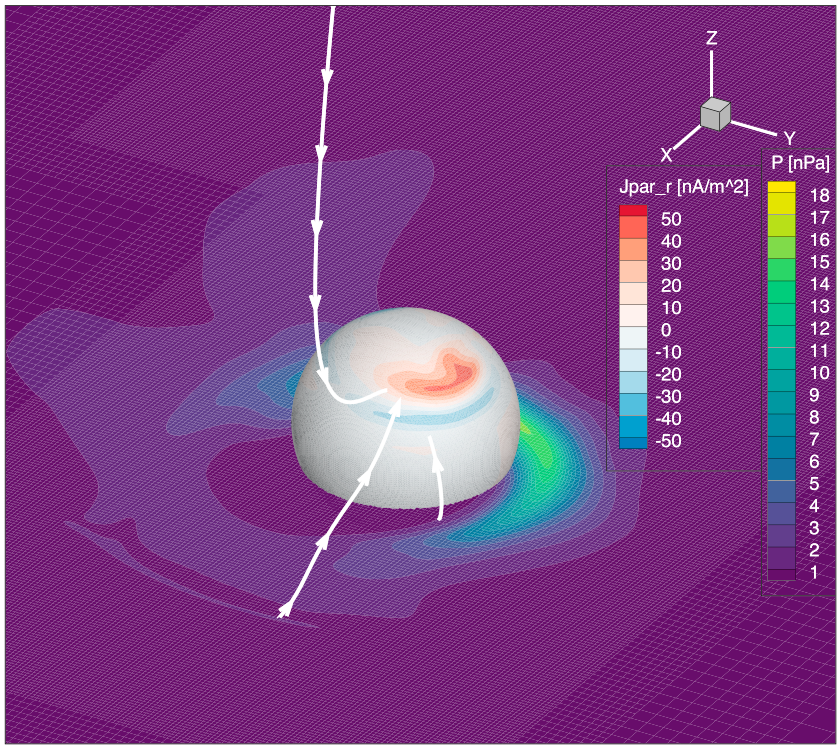

Figure 3. A 3-D view of the simulated magnetosphere extracted from the time step when storm-enhanced density was segmented at 23 UT. Shown in the cut plane XY at $Z = -1$ R_E are color contours of the plasma thermal pressure. Color contours on the sphere with a radius of 3 R_E indicate the field-aligned current density (positive values mean upward field-aligned currents). Three white lines represent the sample magnetic field lines at the storm-enhanced density base (the lowest latitude), boundary flow (the middle latitude), and patch (the highest latitude) around this time. The footprints of these magnetic field lines are shown as stars in Figure 2.

is lower (Heelis et al., 2009; Zou et al., 2013, 2014). This lifting and horizontal advection led to the transport of increased electron density.

At 2130 UT, more plasma was transported from the plasma sheet to the inner magnetosphere due to the steady southward IMF, and the partial ring current developed on the nightside. Because of the increase of the convection electric field, the plasma in the dayside ring current was not in a closed drift path anymore and thus drifted sunward to the magnetopause, which led to the disappearance of ring current on the dayside. Together with continued buildup of ring current on the nightside, the partial ring current formed with larger azimuthal pressure gradient and thus stronger Region 2 FACs according to the Vasyliunas (1970) equation. This led to stronger Region 2 FACs, which flowed up from the dawnside ionosphere and down into the duskside. The partial ring current charged up positive on the duskside and negative in the dawnside to support the Region 2 FAC (Wolf et al., 2007). This charge separation generated a dawnward electric field, which was opposite to the convection electric field. This is referred to as the shielding phenomenon. During this period, the shielding effect began to grow. The electron density in the midlatitude SED base region can continue to grow as long as the convection electric field there is not completely shielded, and a local maximum of electron density is created (see the electron density at 2130 UT in Figure 2). The high-density plasma then drifted further northward and into the polar cap region.

At 2300 UT, the IMF Bz had been steadily southward for 2 hr. A strong partial ring current built up due to the persistent and strong transport from the plasma sheet to the inner magnetosphere. The peak pressure reached ~20 nPa and the pressure gradient generated much stronger Region 2 FACs. Due to the shielding effect, the electric potential was gradually confined to the poleward part of the Region 2 FACs, and the penetrating electric field equatorward of the Region 2 FACs weakened. The direct impact of this electric field pattern change is the formation of intense plasma flows at the boundary between the Region 1 and Region 2 FACs, commonly referred to as the Birkeland current boundary flows (Archer et al., 2017; Archer & Knudsen, 2018). Associated with the boundary flows are increased electric field/velocity gradi-

ents on both sides. The Birkeland current boundary flow may transport the low-density plasma from the nightside to the dayside and also gradually erode the high-density SED plume through enhanced frictional heating. As a result, a patch is segmented from the SED base. It is subsequently transported across the OCB and into the polar cap.

3. Discussion

SED segmentations were previously found to be related with the temporal change of IMF *By* and *Bz* (e.g., Anderson et al., 1988; Milan et al., 2002; Sojka et al., 1993) or transient reconnection (Carlson et al., 2004, 2006; Lockwood & Carlson, 1992). In this case, between 2100 and 2300 UT, both IMF *By* and *Bz* were quite steady, ruling out the possibility of temporal changes of the IMF.

To gain further insight into the magnetospheric origin of convection flows cutting the patch, a 3-D view of the simulated magnetospheric configuration at 2300 UT when the SED is segmented is shown in Figure 3. Color contours of plasma thermal pressure are shown in the cut plane *XY* at $Z = -1\ R_E$. Colors on the sphere at $3\ R_E$ are contours of the FACs (positive values mean upward FACs). Three white lines represent the sample field lines at the center of the SED base (magnetic latitude, MLAT = 57.3, magnetic local time, MLT = 15.0), center of the boundary flows (MLAT = 63.0, MLT = 13.8), and patch (MLAT = 63.5, MLT=13.4). The center of the SED base is where the electron density at 350 km reaches the local maximum, the center of the boundary flow is where the electron density reaches the local minimum, and similarly the center of patch is where the density reaches local maximum. The footprints of these magnetic field lines are marked as white stars in Figure 2. The polar cap patch was on open magnetic field lines and connected to the solar wind, showing that its poleward movement was due to the magnetospheric convection driven by the southward IMF. The SED base was mapped to the inner edge of the partial ring current, where the undershielded electric field was responsible for the SED lifting and TEC growth. This also explains why the SED base stopped providing plasma to the auroral region after the shielding further developed. The boundary flow region was mapped to the outer boundary of the partial ring current (poleward boundary of Region 2 FACs in the ionosphere). This proves that the segmentation was due to the boundary flows located between the Region 1 and Region 2 FACs.

We further investigate how the boundary flows segment the SED plume into a patch. The plasma parcel at the center of the boundary flow at 2300 UT was traced backward in time to 2130 UT to identify its source region. The center of the boundary flow is located at MLAT = 63.0, MLT = 13.8 and marked with a white star in Figure 4c. It is also colocated with the minimum of the electron density. The altitude profile of the electron density at 2300 UT is represented by the blue curve in Figure 4d. When the plasma parcel was traced back in time, it was found that the source region was located at MLAT = 58.3, MLT = 15.6 at 2130 UT and also marked with a star in Figure 4a. The plasma parcel experienced two development phases, that is, a growing phase and a decaying phase. The growing phase started at 2130 UT and continued to 2225 UT. The corresponding altitude profiles of the electron density at these two time cadences are represented by the red and black curves in Figure 4d, respectively. During the growing phase, the plasma was lifted to higher altitudes; that is, the *hmF*2 increased from 270 to 320 km. The lifting was found to be mainly due to projection of the northward convection flows in the vertical direction. At the end of the growing phase, this plasma parcel was located at MLAT = 60.1,MLT = 15.0, indicated by the star near the equatorward boundary of the boundary flow shown in the central panel of Figure 4b. The electron density at the *hmF*2 (~300 km) reached its maximum of 4.09×10^{11} m^{-3} at 2225 UT. The decaying phase started at 2225 UT and the electron density in the *F* layer below 400-km region kept decreasing. The temporal evolution of the horizontal ion drift, electron density, and ion temperature in the plasma parcel at around 350 km is shown in Figures 4e–4g, respectively. The horizontal flow was mainly westward and increased during the whole period due to the constant southward IMF, continuously growing particle ring current and the associated Region 2 current system. The electron density reached the maximum at 2225 UT. After 2225 UT, the convection flow continued to increase, and the ion temperature also increased due to stronger frictional heating between the ions and neutrals, which also resulted in an electron density decrease.

The loss mechanism is further quantified. When the plasma parcel moved from the source region to the boundary flow region, at 300 km (around *hmF*2) the velocity difference between ion and neutral increased

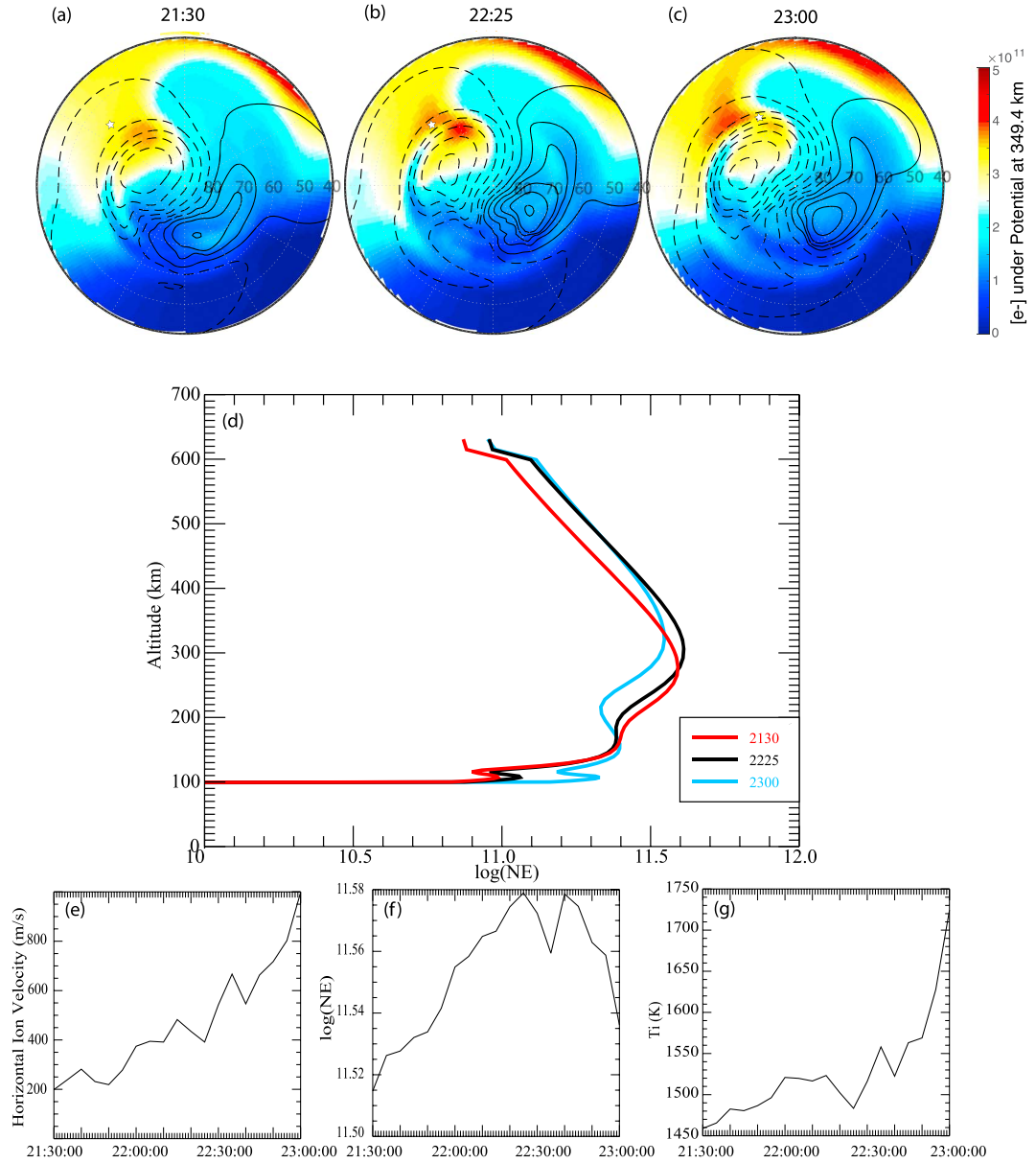

Figure 4. One simulation plasma parcel is traced backward in time. The locations of the plasma parcel and altitude profiles of the electron density at three different time cadences are shown. (a)–(c) Polar view of the *F* region electron density and the locations of the traced plasma parcel are marked with stars at 2130, 2225, and 2300 UT, respectively. The format of polar view plots of the electron density is the same as the second row in Figure 2. (d) The red curve indicates the initial density profile at 2130 UT, the black curve indicates the density profile at the end of the growing phase, that is, 2225 UT, and the blue curve indicates the density profile at the end of the decaying phase, that is, 2300 UT. (e)–(g) The temporal evolution of the horizontal ion drift, electron density and ion temperature in the plasma parcel at around 300 km.

from ~100 to ~600 m/s, the ion temperature increased from ~1400 to ~1700 K, and the neutral temperature remained at ~1400 K. Based on the temperature dependent dissociative recombination equations in St.-Maurice and Torr (1978), the charge exchange rate between O^+ and N_2 increases from 5.73×10^{-13} to 9.91×10^{-13} cm^3/s, when the ion temperature increases from ~1400 to ~1700 K. The N_2 density was $\sim 1.5 \times 10^{14}$ m^{-3}, and O^+ density was $\sim 3 \times 10^{11}$ m^{-3} in the model output. The production rate of NO^+ thus increased 1.88×10^7 m^{-3}/s. The total NO^+ conversion during the decaying phase (~35 min) is 4×10^{10} m^{-3}. Because the recombination between NO^+ and e^- is rapid, the electron density loss should also be 4×10^{10} m^{-3}, which matches the amount of electron lost between 2225 and 2300 UT in the model output. This simple

calculation confirms that the enhanced chemical reaction within the enhanced boundary flows led to the electron density decrease and the segmentation of the SED plume into a patch.

There are several proposed patch segmentation mechanisms with convincing evidence reported in previous literature, which highlights the complicated nature of the high-latitude ionospheric electrodynamics. In this numerical simulation, the partial ring current formed has a single pressure peak, and thus, the associated FAC and flow pattern are relatively simple. However, the ring current can have fine structures (Buzulukova et al., 2010; Wei et al., 2019) and the associated FAC and flow pattern can be more complicated, which can potentially lead to more structures in the segmented patch. A local maximum of the convection flow and a local density minimum at 2235 UT in Figures 4e–4g further confirms this idea.

4. Summary and Conclusions

A new segmentation mechanism of SED plume into polar cap patches is proposed through numerical model study. A simulation of the ionospheric response to the geomagnetic storm on 7 September 2017 has been carried out using the Global Ionosphere and Thermosphere Model (GITM) driven by the two-way coupled BATSRUS and RCM within SWMF. The simulation results are validated by comparison to GPS TEC observations and SYM-H index.

During storm time, dense SED plasma from the midlatitude ionosphere is transported by the expanded two-cell convection pattern into the high-latitude region to form the SED plume. Meanwhile, plasma from the plasma sheet is transported into the inner magnetosphere by strong earthward convection and forms a strong partial ring current centered on the nightside. The partial ring current closes through the Region 2 FACs and gradually shields the subauroral region from the high-latitude penetrating electric fields. As the partial ring current grows, the shielding effect strengthens, causing the boundary flows between the Region 1 and Region 2 FACs to increase. This leads to enhanced ion temperature and chemical recombination rate and thus reduced electron density. When the center of the partial ring current drifts westward due to the gradient and curvature drifts, these large boundary flows also move westward from the nightside to the dayside. When they encounter the SED plume, the plume is segmented into a patch, which later move further into the polar cap. During this process, no IMF variations or transient reconnections are required. The segmentation mechanism is entirely due to magnetospheric internal processes.

Acknowledgments
This work is supported by NASA Grant NNX14AF31G, FINESST19-HELIO19-0021, and NSF Grant AGS1400998. The GPS TEC data used are available at the Madrigal database (http://millstonehill.haystack.mit.edu/). We appreciate Dr. A. Coster for making this data set available for use. The solar wind, IMF, and Sym-H data are obtained from the NASA Omni web. The simulation results for the three selected time cadences are available online (doi:10.7302/9097-z311).

References

Aa, E., Huang, W., Liu, S., Ridley, A., Zou, S., Shi, L., & Wang, T. (2018). Midlatitude plasma bubbles over China and adjacent areas during a magnetic storm on 8 September 2017. *Space Weather*, *16*, 321–331. https://doi.org/10.1002/2017SW001776

Anderson, D. N., Buchau, J., & Heelis, R. A. (1988). Origin of density enhancements in the winter polar cap ionosphere. *Radio Science*, *23*(4), 513–519. https://doi.org/10.1029/RS023i004p00513

Archer, W. E., & Knudsen, D. J. (2018). Distinguishing subauroral ion drifts from Birkeland current boundary flows. *Journal of Geophysical Research: Space Physics*, *123*, 819–826. https://doi.org/10.1002/2017JA024577

Archer, W. E., Knudsen, D., Burchill, J., Jackel, B., Donovan, E., Connors, M., & Juusola, L. (2017). Birkeland current boundary flows. *Journal of Geophysical Research: Space Physics*, *122*, 4617–4627. https://doi.org/10.1002/2016JA023789

Buzulukova, N., Fok, M. C., Pulkkinen, A., Kuznetsova, M., Moore, T. E., Glocer, A., & Rastaetter, L. (2010). Dynamics of ring current and electric fields in the inner magnetosphere during disturbed periods: CRCM-BATS-R-US coupled model. *115*, A05210. https://doi.org/10.1029/2009JA014621

Carlson, H. C., Moen, J., Oksavik, K., Nielsen, C. P., McCrea, I. W., Pedersen, T. R., & Gallop, P. (2006). Direct observations of injection events of subauroral plasma into the polar cap. *Geophysical Research Letters*, *33*, L05103. https://doi.org/10.1029/2005GL025230

Carlson, H. C., Oksavik, K., Moen, J., & Pedersen, T. (2004). Ionospheric patch formation: Direct measurements of the origin of a polar cap patch. *Geophysical Research Letters*, *31*, L08806. https://doi.org/10.1029/2003GL018166

Chamberlin, P. C., Woods, T. N., & Eparvier, F. G. (2007). Flare irradiance spectral model (FISM): Daily component algorithms and results. *Space Weather*, *5*, S05001. https://doi.org/10.1029/2007SW000316

Chamberlin, P. C., Woods, T. N., & Eparvier, F. G. (2008). Flare irradiance spectral model (FISM): Flare component algorithms and results. *Space Weather*, *5*, S07005. https://doi.org/10.1029/2007SW000316

De Zeeuw, D. L., Sazykin, S., Wolf, R. A., Gombosi, T. I., Ridley, A. J., & Tóth, G. (2004). Coupling of a global MHD code and an inner magnetospheric model: Initial results. *Journal of Geophysical Research*, *109*, A12219. https://doi.org/10.1029/2003JA010366

Foster, J. C. (1984). Inospheric signatures of magnetospheric convection. *Journal of Geophysical Research*, *89*(2), 855–865.

Foster, J. C. (1993). Storm time plasma transport at middle and high latitudes. *Journal of Geophysical Research*, *98*(A2), 1675–1689. https://doi.org/10.1029/92ja02032

Fuller-Rowell, T. J., & Evans, D. S. (1987). Height-integrated Pedersen and Hall conductivity patterns inferred from the TIROS-NOAA satellite data. *Journal of Geophysical Research*, *92*(A7), 7606–7618. https://doi.org/10.1029/JA092iA07p07606

Goodwin, L. V., Iserhienrhien, B., Miles, D. M., Patra, S., Meeren, C. V. D., Buchert, S. C., & Moen, J. (2015). Swarm in situ observations of *F* region polar cap patches created by cusp precipitation. *Geophysical Research Letters*, *42*, 996–1003. https://doi.org/10.1002/2014GL062610

Heelis, R. A., Sojka, J. J., David, M., & Schunk, R. W. (2009). Storm time density enhancements in the middle-latitude dayside ionosphere. *Journal of Geophysical Research*, *114*, A03315. https://doi.org/10.1029/2008JA013690

Jin, H., Zou, S., Chen, G., Yan, C., Zhang, S., & Yang, G. (2018). Formation and evolution of low-latitude *F* region field-aligned irregularities during the 7-8 September 2017 storm: Hainan coherent scatter phased array radar and Digisonde observations. *Space Weather*, *16*, 648–659. https://doi.org/10.1029/2018SW001865

Lockwood, M., & Carlson, H. C. (1992). production of polar cap electron density patches by transient magnetopause reconnection. *Geophysical Research Letters*, *19*(17), 1731–1734.

Milan, S. E., Lester, M., & Yeoman, T. K. (2002). HF radar polar patch formation revisited: Summer and winter variations in dayside plasma structuring. *Annales Geophysicae*, *20*(4), 487–499. https://doi.org/10.5194/angeo-20-487-2002

Moen, J., Carlson, H. C., Oksavik, K., Nielsen, C. P., Pryse, S. E., Middleton, H. R., & Gallop, P. (2006). EISCAT observations of plasma patches at sub-auroral cusp latitudes. *Annales Geophysicae*, *24*(9), 2363–2374. https://doi.org/10.5194/angeo-24-2363-2006

Ogawa, T., Buchert, S. C., Nishitani, N., Sato, N., & Lester, M. (2001). Plasma density suppression process around the cusp revealed by simultaneous CUTLASS and EISCAT Svalbard radar observations. *Journal of Geophysical Research*, *106*(A4), 5551–5564. https://doi.org/10.1029/2000JA900111

Oksavik, K., Greenwald, R. A., Ruohoniemi, J. M., Hairston, M. R., Paxton, L. J., Baker, J. B. H., & Barnes, R. J. (2006). First observations of the temporal/spatial variation of the sub-auroral polarization stream from the SuperDARN Wallops HF radar. *Geophysical Research Letters*, *33*, L12104. https://doi.org/10.1029/2006GL026256

Østgaard, N., Vondrak, R. R., Gjerloev, J. W., & Germany, G. (2002). A relation between the energy deposition by electron precipitation and geomagnetic indices during substorms. *Journal of Geophysical Research*, *107*(A9), 1246. https://doi.org/10.1029/2001JA002003

Pinnock, M., Rodger, A. S., Dudeney, J. R., Baker, K. B., Newell, P. T., Greenwald, R. A., & Greenspan, M. E. (1993). Observations of an enhanced convection channel in the cusp ionosphere. *Journal of Geophysical Research*, *98*(A3), 3767–3776. https://doi.org/10.1029/92ja01382

Ren, J., Zou, S., Gillies, R. G., Donovan, E., & Varney, R. H. (2018). Statistical characteristics of polar cap patches observed by RISR-C. *Journal of Geophysical Research: Space Physics*, *123*, 6981–6995. https://doi.org/10.1029/2018JA025621

Ridley, A. J., Deng, Y., & Tóth, G. (2006). The global ionosphere-thermosphere model. *Journal of Atmospheric and Solar-Terrestrial Physics*, *68*(8), 839–864. https://doi.org/10.1016/j.jastp.2006.01.008

Rodger, A. S., Pinnock, M., Dudeney, J. R., Baker, K. B., & Greenwald, R. A. (1994). A new mechanism for polar patch formation. *Journal of Geophysical Research*, *99*(A4), 6425–6436. https://doi.org/10.1029/93JA01501

Shen, C., Luo, B., Chi, Y., Xu, M., & Wang, Y. (2018). Why the shock-ICME complex structure is important: Learning from the early 2017 September CMEs. *The Astrophysical Journal*, *861*(1), 28. https://doi.org/10.3847/1538-4357/aac204

Sojka, J. J., Bowline, M. D., Schunk, R. W., Decker, D. T., Valladares, C. E., Sheehan, R., & Heelis, R. A. (1993). Modeling polar cap *F*-region patches using time varying convection. *Geophysical Research Letters*, *20*(17), 1783–1786. https://doi.org/10.1029/93GL01347

St.-Maurice, J. P., & Torr, D. G. (1978). Nonthermal rate coefficients in the ionosphere: The reactions of O^+ with N_2, O_2 , and NO. *Journal of Geophysical Research*, *83*(A12), 5779. https://doi.org/10.1029/ja083ia12p05779

Tóth, G., Sokolov, I. V., Gombosi, T. I., Chesney, D. R., Clauer, C. R., De Zeeuw, D. L., & Kóta, J. (2005). Space Weather Modeling Framework: A new tool for the space science community. *Journal of Geophysical Research*, *110*, A12226. https://doi.org/10.1029/2005JA011126

Tóth, G., Van der Holst, B., Sokolov, I. V., De Zeeuw, D. L., Gombosi, T. I., Fang, F., et al. (2012). Adaptive numerical algorithms in space weather modeling. *Journal of Computational Physics*, *231*(3), 870–903.

Valladares, C. E., Basu, S., Buchau, J., & Friis-Christensen, E. (1994). Experimental evidence for the formation and entry of patches into the polar cap. *Radio Science*, *29*(1), 167–194. https://doi.org/10.1029/93RS01579

Valladares, C. E., Decker, D. T., Sheehan, R., & Anderson, D. N. (1996). Modeling the formation of polar cap patches using large plasma flows. *Radio Science*, *31*(3), 573–593. https://doi.org/10.1029/96RS00481

Vasyliunas, V. (1970). *Mathematical models of magnetospheric convection and its coupling to the ionosphere* (Vol. 17). Dordrecht: Springer.

Walker, I. K., Moen, J., Kersley, L., & Lorentzen, D. A. (1999). On the possible role of cusp/cleft precipitation in the formation of polar-cap patches. *Annales Geophysicae*, *17*(10), 1298–1305. https://doi.org/10.1007/s00585-999-1298-4

Wei, D., Yu, Y., & He, F. (2019). The magnetospheric driving source of double-peak subauroral ion drifts (DSAIDs): Double ring current pressure peaks. *Geophysical Research Letters*. https://doi.org/10.1029/2019GL083186

Weimer, D. R. (2005). Improved ionospheric electrodynamic models and application to calculating Joule heating rates. *Journal of Geophysical Research*, *110*, A05306. https://doi.org/10.1029/2004JA010884

Wolf, R. A., Spiro, R. W., Sazykin, S., & Toffoletto, F. R. (2007). How the Earth's inner magnetosphere works: An evolving picture. *Journal of Atmospheric and Solar-Terrestrial Physics*, *69*(3), 288–302. https://doi.org/10.1016/j.jastp.2006.07.026

Zhang, Q. H., Moen, J., Lockwood, M., McCrea, I. W., Zhang, B. C., McWilliams, K. A., & Lester, M. (2016). Polar cap patch transportation beyond the classic scenario. *Journal of Geophysical Research: Space Physics*, *121*, 9063–9074. https://doi.org/10.1002/2016JA022443

Zhang, Q. H., Zhang, B. C., Liu, R. Y., Dunlop, M. W., Lockwood, M., Moen, J., & Lester, M. (2011). On the importance of interplanetary magnetic field By on polar cap patch formation. *Journal of Geophysical Research*, *116*, A05308. https://doi.org/10.1029/2010JA016287

Zhang, Q. H., Zhang, B. C., Moen, J., Lockwood, M., McCrea, I. W., Yang, H. G., & Lester, M. (2013). Polar cap patch segmentation of the tongue of ionization in the morning convection cell. *Geophysical Research Letters*, *40*, 2918–2922. https://doi.org/10.1002/grl.50616

Zou, S., Moldwin, M. B., Ridley, A. J., Nicolls, M. J., Coster, A. J., Thomas, E. G., & Ruohoniemi, J. M. (2014). On the generation/decay of the storm-enhanced density plumes: Role of the convection flow and field-aligned ion flow. *Journal of Geophysical Research: Space Physics*, *119*, 8543–8559. https://doi.org/10.1002/2014JA020408

Zou, S., Ridley, A. J., Moldwin, M. B., Nicolls, M. J., Coster, A. J., Thomas, E. G., & Ruohoniemi, J. M. (2013). Multi-instrument observations of SED during 24–25 October 2011 storm: Implications for SED formation processes. *Journal of Geophysical Research: Space Physics*, *118*, 7798–7809. https://doi.org/10.1002/2013JA018860